Simulating complex conductivity in carbonate rocks: using digital carbonate rocks and

comparison to laboratory measurements

By

James Colgin

B.Sc., University of Texas of the Permian Basin, 2016

B. Sc., University of Texas at Austin, 2010

Submitted to the graduate degree program in the Department of Geology and the Graduate

Faculty of the University of Kansas in partial fulfillment of the requirements for the degree of

Master of Science, Geology.

_____

Chair: Chi Zhang, Ph.D.

_____

George Tsoflias, Ph.D.

_____

Xianglin Li, Ph.D.

Date Defended: 28 November 2018

The thesis committee for James Colgin

certifies that this is the approved version of the following thesis:

Simulating complex conductivity in carbonate rocks: using digital carbonate rocks and

comparison to laboratory measurements

_____

Chair: Chi Zhang, Ph.D.

Date Approved: 28 November 2018

ABSTRACT

Digital rock physics involves the modern microscopic imaging of geomaterials, digitalization of the microstructure, and numerical simulation of physical properties of rocks. This physics-based approach can give important insight into understanding properties of reservoir rocks, and help reveal the link between intrinsic rock properties and macroscopic geophysical responses. Our focus is the simulation of the complex conductivity of carbonate reservoir rocks using reconstructed 3D rock structures from high-resolution X-ray micro computed tomography (micro-CT). Carbonate core samples with varying lithofacies and pore structures from the Cambro-Ordovician Arbuckle Group and the Upper Pennsylvanian Lansing-Kansas City Group in Kansas were used in this study. The wide variations in pore geometry and connectivity of these samples were imaged using micro-CT. A two-phase segmentation method was used to reconstruct a digital rock of solid particles and pores. We then calculated the effective electrical conductivity of the digital rock volume using a pore-scale numerical approach. The complex conductivity of geomaterials is influenced by the electrical properties and geometry of each phase, i.e., the solid and fluid phases. In addition, the electrical double layer that forms between the solid and fluid phases can also affect the effective conductivity of the material. In the numerical modeling, the influence of the electrical double layer is quantified by a complex surface conductance and converted to an apparent volumetric complex conductivity of either solid particles or pore fluid. The effective complex conductivity resulting from numerical simulations were compared to results from laboratory experiments on equivalent rock samples. In general, simulated σ'_{eff} values were below laboratory measurements, while numerical σ''_{eff} values were within reasonable range. The imaging and digital segmentation

technique, fundamental rock characteristics, and model assumptions all play an important role in the simulation process.

ACKNOWLEDGEMENTS

TABLE OF CONTENTS

INTRODUCTION

Macroscopic geophysical measurements are governed by pore-scale rock properties. Understanding pore-scale structures and processes of rocks is necessary to fully interpret laboratory and field geophysical observations. Current geophysical interpretations rely on models that attempt to connect geophysical measurements with geological properties of interest. These models assume a simplified microstructure; however, real rocks are intrinsically heterogeneous and complex, especially shales and carbonates. Carbonate rocks contain a significant amount of hydrocarbon resources and form many important water-bearing zones. Our goal is to explore how pore-scale geometry of these complicated rocks control the complex electrical conductivity, which can be used to reveal pore structure as well as fluid-rock interactions in carbonate rocks in order to help us better understand various geological processes. We achieve this goal by using emerging digital rock physics techniques and previously defined electrochemical models that explain complex conductivity in porous media.

Digital rock physics involves high-resolution 3D imaging of a real samples, digitization of the microstructure, and computation of macroscopic properties (Andrä et al. 2013a, b). The use of digital rock physics as a research tool has grown over the past few decades with the increase in computing power. A wide range of studies exist for sandstones, shales, carbonates, and unconsolidated material. Most of these studies focus on fluid transport and acoustic attenuation (Knackstedt et al. 2009, Vanorio and Mavko 2011, Quintal et al. 2011) with a sizable amount of studies on electrical conductivity (or resistivity) and formation factor (Yan et al. 2016, Sengupta, Kittridge, and Blangy 2017) and even fewer incorporating the effects of the electrical double layer and surface conductance (Shabro et al. 2014). In the nomenclature of geophysics,

1

digital rock physics takes the forward modeling approach to understand scientifically and societally important topics such as contaminant transport, CO_2 sequestration, and reservoir characterization.

Our study entails the computation of the effective (bulk) complex conductivity of digital carbonate reservoir rock volumes and a comparison to laboratory measurements. The complex electrical response of geomaterials can be measured by the induced polarization (IP) method in the field and laboratory (Kemna et al. 2012) and is influenced by the electrical properties of the solid and fluid phases, the geometry of the microstructure, and the electrical double layer that forms at the solid-fluid interface (Revil, Florsch, and Camerlynck 2014). The IP method is especially sensitive to internal surface area, connectivity, and fluid chemistry. The interpretation of laboratory or field data can lead to the estimation of pore size distributions (Florsch, Revil, and Camerlynck 2014), contaminant plume mapping (Sogade et al. 2006), and microbial activity monitoring (Davis et al. 2006). Our study specifically explores how pore-scale rock parameters (i.e., surface charge density Q and dynamic pore radius Λ), pore size distributions based on extracted pore network models, and micro-CT imaging resolutions can affect the simulated bulk conductivity response of our digital rocks. We then compare the simulated values to spectral induced polarization (SIP) laboratory results measured on the same samples.

METHODS

Workflow and Sample Selection

2

The workflow for this study is depicted in Figure 1. Our process involved micro-CT scanning, processing and 3D reconstruction, solid and fluid phase segmentation, connectivity analysis, pore network extraction, the application of induced polarization in the electrical double layer to the digital microstructure, and finally the effective conductivity calculation of the bulk volume. Twelve samples were scanned in this study. The core plugs were predominantly carbonate in mineralogy and obtained from various formations in Kansas. Eight grainstones, mostly oomoldic, were from the Lansing-Kansas City Group (Upper Pennsylvanian in age); two packstones and two mudstones were from the Arbuckle Group (Cambro-Ordovician in age). Helium porosities and Klinkenberg-corrected air permeabilities were previously measured through routine core analysis by a commercial laboratory. Our samples were chosen over a wide range of porosities (~ 3% – 33%) and permeabilities (~ 0.01 mD – 200 mD). Detailed sample information is listed in Table 1.

CT Scanning and Reconstruction

Our study used X-ray micro-computed tomography (micro-CT) scanning technology to obtain three-dimensional digital rock volumes. X-rays travel through the sample and refract according to Snell's law. The resulting image intensity is high (bright) in areas where x-rays are converging, and vice-versa for low intensity (darker) areas. The detector measures the phase contrast. In effect, brighter regions indicate harder rock parts, and darker regions indicate softer rock parts and pores. This brightness contrast is the basis for identifying solid versus pore regions during the segmentation process. We cut the core plugs into thin sticks (roughly 1.5 mm – 3.5 mm thick) to prepare for micro-CT scanning. We used microscope lenses with two

3

different optical magnifications, 10X and 4X, to explore different resolutions over the samples using the phase contrast micro-CT Xradia MicroXCT-400 microscope at the University of Kansas Institute for Bioengineering Research (IBER). Magnification levels and resolutions are included in Table 1. There is a trade-off between the magnification level and the effective volume that can be scanned; higher resolution scans cover a smaller 3D sample volume. The microscope software outputs the raw data images as a sequence of 2D slices in grayscale. The intensity value of each pixel ranges from 0 (darkest) to 255 (lightest). Roughly 1000 image slices with dimensions of 1000×1000 pixels were acquired for each sample. A 600×600 pixel area, centered on the axis of the sample, was then cropped out of each slice, and the 600 middle slices were then compiled together sequentially to form a 600^3 digital array using a MATLAB script that we created.

The reconstructed digital volumes from micro-CT scanning revealed the varying levels of diagenesis, different pore structures, and connectivity characteristics of our samples. Certain cementation and harder material, most likely metallic minerals such as pyrite, were visible in some of the samples. For example, sample G2 contained larger shell fragments and fossils. Sample G6, a skeletal grainstone from Upper-Pennsylvanian Lansing-Kansas, was characterized by intergranular porosity and contained pellets, some of which were partly dissolved. There appeared to be good connectivity surrounding the pellets and between some of the larger grains. Most of our grainstones were oomoldic in nature and contained many large dissolved pores, but some samples also contained a small amount of only partly dissolved ooids. The large spherical pore spaces sometimes overlapped or connected via smaller cracks.

Phase Segmentation

A two-phase thresholding method was used to segment the image cubes into solid and pore regions. To do this, a grayscale value was chosen for each sample that distinguished a solid voxel from a pore voxel. Because each sample has different hardness, density, and cementation characteristics, there are slight differences in the micro-CT scanning results and therefore the threshold was tailored for each sample. To help choose the ideal threshold, an intensity histogram, generated from a MATLAB script that we created, was analyzed for each sample to identify the darker regions (pores) from brighter regions (solid). The first and second peaks indicate clusters of pore and solid intensity values, and a threshold value is chosen between these peaks to partition the two phases. For quality control, a raw CT slice is compared to a segmented slice to visually check that the solid-pore boundary is maintained with the chosen threshold value. This value ranged from 105 to 145 for our samples.

Post-Processing

Following segmentation, we then compressed, or re-gridded, each 600^3 digital cube into a 200^3 cube in order to reduce computer demand and computation times but maintain the same effective sample volume. To do this, each original cube was partitioned into smaller cubes of 27 voxels. Within each smaller cube, we looked to see how many pore voxels were present out of 27. If this value was above a user-given criterion number, then we defined a new single pore voxel. If there weren't enough pore voxels within the smaller cube, then we defined a new single solid voxel. In effect, we decreased the total number of voxels to process for each image cube from 600^3 voxels to 200^3 voxels to expedite our later calculation for electric current flow. Ideally,

5

the compression criterion number is chosen so that the final porosity of the digital structure is comparable to the helium porosity. A minimum compression criterion value of 3, which could be interpreted as a straight path across each smaller partitioned cube, can be used to represent the most relaxed option for this processing step. Higher numbers require more pores to be present within each partitioned cube in order to re-grid to a single pore voxel. To investigate how our data compression method affected sample porosity, connectivity, and electrical conductivity, we generated multiple microstructures with different compression criterions for each sample ranging from 10 to 3. A summary of the compression criterion numbers used for each trial in this study is included in Table 2.

Connectivity Analysis

Once the final digital structure has been compiled, we then tested if the fluid phase percolates through the microstructure of each image cube. A digital sample is connected if a given phase percolates through microstructure, from one cube face to the opposite face. A connected sample has at least one pathway that begins with a cell on the cube edge and connects to the other edge through cells of the same phase. Because the pore fluid and the pore-solid boundary are the conducting regions, we checked to see if the pore phase was connected in our samples in all three directions. To do this, we used a burning algorithm developed by the National Institute of Standards and Technology (Garboczi 1998) (available at https://ciks.cbt.nist.gov/garbocz/manual/node59.html). Only five out of the original twelve samples were tested as well connected, having the pore phase percolating through the sample in at least two axis directions. We continued our investigation of these five samples only. Their

micro-CT reconstructions are shown in Figures 2 – 6. These images show the original micro-CT reconstructions with 600 stacked images on each sample and a cube edge of ~ 2.6 mm.

Pore Network Extraction

We generated pore network models using an algorithm developed by the Imperial College London to extract information on the pore size distribution and obtain pore network models of our microstructures. This maximal ball algorithm works by filling the pore space with spheres inscribed within the solid-pore boundary. Large spheres near the center of pore regions become nodes. Chains of smaller spheres that connect larger nodes become cylindrical tubes (Dong and Blunt 2009). The extracted sphere and tube models were plotted to visualize the pore space and connectivity of each sample. From this simplified pore network, we were able to extract information on pore radii and pore throats and their volumes. Pore sizes were binned into 30 groups and pore size distributions were plotted alongside their pore network models for each sample in Figures 7 – 11.

The heterogeneity and complexity of our samples became more apparent after generating these models. As expected, sample M2, the mudstone had the smallest node and tube radii compared to the other samples. Sample G6, the skeletal grainstone, exhibited slightly larger node radii than the mudstone, but similar tube radii. It also consisted of the highest number of tubes and therefore had the highest degree of connectivity of all the samples. Samples G4, G2, and G1, the oomoldic grainstones, were comprised of mostly vary large node sizes and large to small tubes. For all samples, there were entire regions where there were no nodes or tubes generated. These are areas with high solid concentrations which hinder connectivity across the sample.

7

There were also regions where the algorithm generated very dense clusters of small nodes and tubes compared to the rest of the sample. These clusters appear in areas with only partly dissolved ooids or a high concentration of pellets.

Application of the Electrical Double Layer Model and Induced Polarization Response

After constructing our digital rock volumes and obtaining pore size information, we then moved to the next step in the simulation workflow. The set-up to the numerical bulk conductivity calculation first begins by assigning local conductivity values for the solid and fluid voxels. To do this, we adopted a "pore upscaling" method (Niu and Zhang 2017) to account for electrical conduction and polarization effects, which converts the complex surface conductance to an apparent volumetric conductivity in the fluid phase.

Geomaterials exhibit a complex conductivity when subjected to an electric field in which the real part describes energy loss and the imaginary part describes energy storage:

$$\sigma^* = \sigma' + i\sigma'' = \sigma' + i\varepsilon_r\varepsilon_0\omega \tag{1}$$

where σ^* represents the complex conductivity of the material, σ' and σ'' are the real and imaginary components, i is the imaginary unit, ε_r is the relative permittivity of the medium, ε_0 is the permittivity of free space, and $\omega = 2\pi f$ is the angular frequency. In addition to electrical conduction in the bulk solution, geomaterials experience conduction and polarization in the electrical double layer at the solid-fluid interface. To account for these effects, conductivity values are assigned to the two phases in the following manner:

$$\sigma_w^* = \sigma_w' + i\varepsilon_w\varepsilon_0\omega + \Delta\sigma_w^* \tag{2}$$

$$\sigma_s^* = \sigma_s' + i\varepsilon_s\varepsilon_0\omega \tag{3}$$

8

where σ_w^* and σ_s^* are the apparent complex conductivity of the fluid and solid phase, and $\Delta\sigma_w^*$ is the additional complex conductivity gained to the fluid phase due to the effects of the electrical double layer. This value is defined as:

$$\Delta\sigma_w^* = \frac{2}{\Lambda} \cdot C_S^* = \frac{2}{\Lambda} \cdot (C_S^0 + C_S^s) \tag{4}$$

where C_S^* is the electrical double layer-induced complex surface conductance, and Λ is the dynamic pore radius (Johnson, Koplik, and Schwartz 1986). C_S^* is the combined influence from the diffuse layer C_S^0 and Stern layer C_S^s. For the diffuse layer:

$$C_S^0 = \beta \cdot Q \tag{5}$$

where β and Q are the ion mobility and surface charge density related to the diffuse layer. The Stern layer exhibits simple Debye relaxation, a special case of Cole-Cole relaxation (Schwarz 1962):

$$C_S^s = \sum_{i=1}^n f_i \frac{i\omega\tau_i}{1 + i\omega\tau_i} \beta \cdot Q \tag{6}$$

where β and Q are the ion mobility and surface charge density related to the Stern layer, w_i is a weighting function, τ_i is the relaxation time. For geomaterials comprised of different pore sizes, each pore size has a contribution to the complex conductivity response (Leroy et al. 2008). The weighting function and relaxation time are a function of pore size r_i obtained from the binned pore size distribution data. Each pore size has a volume v_i that is weighted from the total pore space volume, and each weight sums to 1:

$$Total\ Pore\ Volume = \sum_{i=1}^n v_i \tag{7}$$

$$\sum_{i=1}^n \frac{v_i}{Total\ Pore\ Volume} = \sum_{i=1}^n f_i = 1 \tag{8}$$

9

where n is the number of pore sizes. The relaxation time τ_i is related to the curvature of the electrical double layer:

$$\tau_i = \frac{r_i^2}{2D} \tag{9}$$

where D is the diffusion coefficient in the Stern layer. The radius of the electrical double layer is equivalent to the pore radius (Schwarz 1962). Note that it was assumed that the surface charge densities Q associated with the diffuse and Stern layer are equal (Niu and Zhang 2017).

For inputs to our numerical simulations, we chose $\sigma_w' = 0.12$ S/m to match our laboratory fluid conductivity. Other parameters followed previously reported values (Niu, Revil, and Saidian 2016, Niu et al. 2016): fluid permittivity $\varepsilon_w = 80$; $\sigma_s' = 0$ (no conduction in the solid phase); permittivity of calcite $\varepsilon_s = 8$; permittivity of free space $\varepsilon_0 = 8.854 \times 10^{-12}$ F/m; ion mobility of Na$^+$ in the diffuse and Stern layers $\beta = 5.2 \times 10^{-12}$ m^2/sV; diffusion coefficient $D = k_b T \beta^s / e$ with Boltzmann constant $k_b = 1.3806 \times 10^{-23}$ J/K, room temperature $T = 293.15$ K, and elementary charge $e = 1.602 \times 10^{-19}$ C. For simulation purposes, the Λ parameter was altered from $20 - 100$ nm (Oyewole, Saneifar, and Heidari 2016, Duan et al. 2018) and the Q parameter was altered from $3 \times 10^{-4} - 8 \times 10^{-4}$ C/m^2 (Niu, Revil, and Saidian 2016) which are acceptable ranges for carbonate rocks. We performed the simulation over the 1 mHz $- 1$ kHz range.

Our definitions above allowed us to account for the complex conductivity of the solid and fluid phases and the additional complex surface conductance due to the effects of the electrical double layer, are based on pore sizes obtained from digital reconstructions of real carbonate rocks, and are frequency-dependent. Table 2 provides a summary of the simulation trials in this study and the specific values chosen for the Λ and Q parameters during the set-up to the effective conductivity calculation.

Numerical Calculation of σ_{eff}^*

Each voxel at position $\boldsymbol{x} = (x, y, z)$ where x, y, and z are the coordinates is defined by its

phase state (solid or fluid) and its local complex conductivity $\sigma^*(\boldsymbol{x})$ according to the above

section's definitions. We then simulated current flow I through the digital sample resulting in

potential difference ΔP across it. We calculated the average electric field $\langle \boldsymbol{E} \rangle$ and current density

$\langle \boldsymbol{J} \rangle$ to determine the effective complex conductivity of the bulk sample σ_{eff}^*:

$$\sigma_{eff}^* = \frac{\langle \boldsymbol{J} \rangle}{\langle \boldsymbol{E} \rangle}. \tag{10}$$

$\langle \boldsymbol{E} \rangle$ and $\langle \boldsymbol{J} \rangle$ are functions of position $\boldsymbol{x}$ and are defined by (Mendelson 1975, Cheng and Torquato

1997):

$$\langle \boldsymbol{E} \rangle = -\frac{1}{V} \int_V \nabla \Psi(\boldsymbol{x}) \, dV \tag{11}$$

$$\langle \boldsymbol{J} \rangle = \frac{1}{V} \int_V \boldsymbol{J}(\boldsymbol{x}) \, dV \tag{12}$$

where V is the sample volume, $\boldsymbol{J}(\boldsymbol{x})$ is the local current density, and $\Psi(\boldsymbol{x})$ is potential. Local

current density and potential were solved by the Laplace equation:

$$\nabla \boldsymbol{J}(\boldsymbol{x}) = 0 \tag{13}$$

$$-\nabla[\sigma^*(\boldsymbol{x}) \nabla \Psi(\boldsymbol{x})] = 0. \tag{14}$$

These calculations were performed numerically using code developed by the National Institute of

Standards and Technology (available at https://ciks.cbt.nist.gov/garbocz/manual/node57.html).

For more information on the algorithm, see Garboczi (1998). The code solves the finite

difference representation of the Laplace equation with the conjugate gradient method.

RESULTS AND DISCUSSION

An analysis of our simulation results and a discussion on the methods follows. After performing the effective conductivity simulations, results were compared to laboratory SIP measurements previously made on the original core plugs. We demonstrate several key factors that impact the complex conductivity simulation in carbonate rocks. We will discuss the limitations of micro-CT scanning, which is a common issue with image-based analysis methods; the impact of using the maximal ball pore network models and the parameters derived from them, such as the curvature of the electrical double layer r_i, relaxation time τ_i, and the complex conductance of the Stern layer C_S^s; and the user-chosen inputs for other pore-scale parameters – the dynamic pore radius Λ and surface charge density Q.

The simulated σ'_{eff} and σ''_{eff} values for each trial, along with laboratory data, is included Figures 12 – 16. In general, the simulated σ'_{eff} underestimated laboratory measurements, but the simulated σ''_{eff} were a decent match in the lower- to mid-frequencies. In addition, formation factor F and cementation exponent m values derived from the simulation results were overestimated when compared to the SIP laboratory-derived values. The effects of the pore-scale parameters Λ and Q, and our compression criterion used during the image processing, can be seen in the shifts to the simulated σ'_{eff} and σ''_{eff} curves between trails. A more detailed analysis of these parameters follows in their respective sections.

A notable difference between the σ''_{eff} simulation versus measured curves is the overall shape of the spectra. In general, the laboratory measurements exhibit a flat curve without a characteristic frequency, whereas the simulation results have peaks in the lower frequencies.

Previous studies have argued that a flat spectrum could be due to a rough grain surface (Leroy et al. 2008). Therefore, it is possible due to the limitations in scanning resolution and post-processing re-gridding that the rough quality of the grain surface was smoothed out on the digital structures. The peak in our simulation results is due to the electrical double layer polarization mechanism that we assumed in our model. However, there may be other polarization models or physical explanations reflected in the laboratory measurements that we did not address in our simulation. For example, membrane polarization is another polarization mechanism that explains polarization effects due to variable pore throat sizes (Marshall and Madden 1959, Bücker and Hördt 2013). Maxwell-Wagner effect (dielectric polarization) could exist in porous media at higher frequencies (Leroy et al. 2008, Chen and Or 2006). It is possible that a model incorporating membrane polarization effects combined with electrical double layer polarization at the grain-fluid boundary may better predict the IP response in complicated rocks like carbonates.

EFFECTS OF IMAGE RESOLUTION AND PROCESSING

Digital rock physics entails a collection of various methods and issues arising from the chosen techniques. Choosing a simple intensity threshold may not be the best method, as variations in mineral density and scanning resolution complicate intensity histograms. A kriging segmentation method has been shown to be superior to simple thresholding (Sakellariou et al. 2003, Lindquist et al. 2000). A watershed segmentation method may also be used on high-resolution images to better discern the solid-pore boundary (Saenger and Madonna 2011). Simple intensity thresholding tends to cause separate grains to appear as one connected mass;

13

this could explain why more than half of the digital microstructures from our initial sample group were not connected in any direction. Maintaining pore space between grains from imaging techniques has clear implications on discerning pore throats and electrical conductivity simulations. Alternative methods in machine learning and statistical reconstructions from 2D images have also been employed in the realm of digital rock physics (Tang and Spikes 2017, Al-Kharusi and Blunt 2008, Karimpouli and Tahmasebi 2016).

In addition to segmentation considerations, the scanning resolution and grid spacing must correctly represent the properties of the real rock microstructure (Keehm and Mukerji 2004, Bazaikin et al. 2017). This is known as the representative elementary volume (REV) concept – that a digital or simulated rock property must be statistically representative of the bulk sample. Simulations are affected by variables like scanning resolution and grid spacing, and it is possible that a model based on digital microstructures over- or under-estimates a physical process or pore-scale geometry. Although there is a trade-off between resolution and effective volume scanned, higher resolution images are preferred but difficult to obtain in practice. This is especially true for carbonates in particular because these rocks exhibit a wide variation in pore networks and pore types at different scales. Studies show that more pore space is resolved at higher resolutions, but porosities based on imaging methods will fall short of measured helium porosities (Sakellariou et al. 2003). Our results indicated this as well, and overall, our numerically calculated σ'_{eff} and σ''_{eff} values under-estimated laboratory measurements, with the greatest discrepancy arising from the mudstone. We can assume that the fine-grained nature and pore space of this rock type was more difficult to capture than the grainstones at our resolution (4.30 µm). Any nanoporosity in the mudstone sample was missed by the micro-CT scanning, as these pore sizes were outside of the detection range. It may not be possible for micro-CT

14

imaging to resolve the porosity of some fine-grained carbonate rocks, but approximation methods can be devised that are calibrated with micro-CT measurements that utilize more than two phases during segmentation, for example, an intermediate phase (Saenger et al. 2014). Injection of a high-salinity brine before micro-CT scanning can also detect sub-resolution porosity in carbonate cores (Lin et al. 2016). Furthermore, there are higher resolution imaging techniques such as SEM, FIB-SEM, and BIB-SEM that can identify nanoscale pores. However, the issue of whether or not these higher resolution techniques can produce a proper REV for fine-grained rocks still remains (Kelly et al. 2016).

In our workflow, we re-gridded the digital samples from 600^3 voxels to 200^3 voxels. Decreasing the number of voxels to process from 600^3 to 200^3 exponentially cut down on processing times. The compression criterion number, which controls how strict the algorithm is when re-gridding the solid and pore regions, can be tailored to produce a final digital microstructure with a porosity that is agreeable to laboratory helium porosities. In a way, this enables us to "make up" for lost porosity due to micro-CT and segmentation limitations. However, there are some concerns if this step maintains an REV or not. Again, under-estimation of porosity due to micro-CT methods is a common problem (Sakellariou et al. 2003), but our approach is one attempt at circumventing the issue.

The compression criterion number for samples M2, G6, and G4 were altered in our study. Results for trial M2-A and M2-B illustrate how changing only this value can impact porosity, σ'_{eff}, and σ''_{eff}. A strict compression criterion number of 10 for M2-A generated a microstructure with a lower porosity (11.7%) than a more lenient compression criterion number of 3 for M2-B (15.6%). More pore space, a higher total surface area, and a higher number of pathways are maintained within the final processed microstructure by lowering this criterion number.

Therefore, σ'_{eff} and σ''_{eff} are higher at all frequencies. Similar results can be seen when comparing trials G6-B to G6-A. However, in trial G6-C, increasing Q had a more influential impact than the compression criterion number on σ''_{eff} and did not considerably affect σ'_{eff}. Similarly, results for trials G4-A and G4-B showed that increasing Λ had a greater impact on σ''_{eff} (and did not affect σ'_{eff}).

EFFECTS OF PORE-SCALE SIMULATION PARAMETERS

In the simulation, a number of variables are used as inputs to model pore-scale rock properties and the effects of the electrical double layer at fluid-rock interfaces. Some of these parameters are difficult to measure experimentally and can only be perceived conceptually. Determining these parameters is important because it helps us understand the macro-scale electrical behavior of rocks and the issues with upscaling. In our study, we explored determining pore size distributions using pore network models. We focused on the effects of the dynamic pore radius Λ and surface charge density Q. The value of these parameters can significantly impact simulation results.

Pore Network Modeling

The pore network models in our study were generated using the maximal ball algorithm discussed in the "pore network extraction" section (Dong and Blunt 2009). This algorithm generated the sizes and locations of pore nodes (spheres) and pore throats (tubes) encompassed within the pore phase of the digital microstructure. The extracted network represents a simplified

model of the imaged pore space. Pore-scale flow simulations based on these maximal ball

models (Mahabadi et al. 2016) are typically performed instead of direct calculations on the

digital pore space as they are computationally faster. These simulations are able to predict

permeability and capillary pressure well, but can underestimate other features that were directly

calculated on the pore space (Dong and Blunt 2009). There is also some concern of whether or

not these maximal ball networks oversimplify the real structure by losing some details,

particularly the smaller-sized connectivity compared to the rest of the network (Blunt et al.

2013), which is particularly present in more complex samples such as carbonates.

In our study, the pore networks generated from the maximal ball approach helped to

quantify a pore size distribution for our samples. Pore size distributions are important to pore-

scale rock characterization and can be measured using laboratory methods such as mercury

injection capillary pressure (MICP) (Scott and Barker 2003, Niu and Revil 2015), SIP, and

nuclear magnetic resonance (NMR) (Niu and Zhang 2018). The pore size distribution data

extracted from our pore network models was used to mathematically define pore sizes r_i and

their respective weights f_i. This information was carried through in the electrical double layer

and induced polarization modeling by affecting values for the radius of the curvature of the

electrical double layer (equated to r_i), the relaxation time τ_i, and the influence of the complex

surface conductance induced in the Stern layer C_S^s. It is important to note our separate use of the

pore size distribution r_i and the dynamic pore radius Λ. There are studies that do in fact equate

these two values (Revil, Florsch, and Camerlynck 2014, Niu and Revil 2015) and others that use

a grain size parameter when defining relaxation times (Revil, Koch, and Holliger 2012). Many of

these studies assume spherical grains, which may not be realistic for our more complex

carbonate samples. For our study, we wanted to obtain a representation of the pore size based on

image analysis, so we decided to extract this information from the maximal ball pore networks and equate it to r_i. This allowed us to characterize the general shape of the pore size distribution, but as discussed earlier, much of the sub-resolution porosity is lost during the imaging process. Therefore, we kept the Λ parameter (discussed below) as a user-defined value in the simulation. It could prove beneficial to supplement pore size estimates based on image analysis alone with laboratory MICP measurements to more accurately represent the full distribution and hopefully lead to a better prediction of the induced polarization effects. Pore network extractions on digital carbonates rocks can be poorly connected due to the resolution issue (Dong and Blunt 2009), and as discussed earlier, image-based methods will underestimate porosity (Sakellariou et al. 2003). Therefore, we assume there is some degree of inaccuracy in representing these real values due to resolution and processing limitations. This could explain why the simulated behavior of the mudstone sample showed the greatest deviation from laboratory measurements, as there may be considerable pore space below our resolution limits.

Dynamic Pore Radius Λ

The parameter Λ is sometimes referred to as the "characteristic" pore size – it is linked to the pore-scale geometry of the medium and to the conducting regions at the grain-fluid interface. Studies on fluid flow in porous materials commonly make use of a hydraulic pore radius, defined as V_p/S, in Kozeny-Carmen equations. Λ can be defined as weighted version of the hydraulic pore radius, weighted by the norm of the electric field in the pore space before the formation of the electrical double layer (Revil, Koch, and Holliger 2012). It represents the radius of interconnected pores that control fluid and electrical transport phenomena in porous media.

Transport is dominant in large, connected pore throats. Λ is inversely related to the formation factor F and surface area-to-pore volume ratio S/V_p (Johnson, Koplik, and Schwartz 1986). In the modeling, Λ is included in the denominator of our definition of the complex conductivity of the pore fluid, $\Delta\sigma_w^*$. Therefore, a smaller Λ will translate to a larger induced complex conductivity. This inverse relationship exists because smaller pores represent samples with a rougher texture and a higher surface area (Revil, Florsch, and Camerlynck 2014) leading to more surface sites where charge build up can occur. Therefore, rocks comprised of smaller pores will exhibit more significant polarization than those with larger pores and of the same lithology. This is especially helpful in characterizing the differences in complex rocks such as carbonates.

As mentioned earlier, the Λ parameter can be obtained experimentally from MICP measurements. We do not have MICP data, however for simulation purposes we substituted values within a range previously measured for carbonate reservoir rocks (Oyewole, Saneifar, and Heidari 2016, Duan et al. 2018). Only Λ was altered for trials G2-A (Λ = 100 nm), G2-B (Λ = 50 nm), and G2-C (Λ = 20 nm). Results showed that σ'_{eff} was not significantly affected by this value, but σ''_{eff} increased as Λ decreased. Similar results were shown when Λ was altered for trials G4-A (Λ = 20 nm) and G4-B (Λ = 100 nm). As expected, a smaller Λ input in our simulations led to a more significant polarization effect (Figure 14, Figure 15). As mentioned earlier, it might be possible to append the image-generated pore size data with MICP measurements in order to more accurately predict the induced polarization response.

It is important to note that there is some disagreement on whether a pore size or grain size parameter controls induced polarization behavior and relaxation times (Revil, Koch, and Holliger 2012, Revil 2013). Our study utilized pore size parameters in the simulations, but it is entirely possible to devise a workflow based on image analysis and using grain size input variables.

Surface Charge Density Q

The surface charge density Q is a physical concept that describes the amount of charge buildup at the solid-fluid interface. It is affected by the mineralogy of the grain, the electrolyte concentration, and the pH. It can be measured in the laboratory by potentiometric titrations and confirmed by streaming zeta potential experiments (Revil and Glover 1997, Revil, Pezard, and Glover 1999, Walker and Glover 2018). A higher Q implies a greater number of surface charge sites, which enhances electrochemical interactions at the solid-fluid interface and strengthens the polarization effect (Niu, Revil, and Saidian 2016, Niu and Revil 2015). In the modeling, a higher Q leads to an increased complex conductance in the diffuse layer C_S^0 and Stern layer C_S^s, ultimately producing a higher complex conductivity in the fluid phase voxels $\Delta\sigma_w^*$. In our modeling, we assumed that the charge densities associated with Stern and diffuse layers were equivalent. To maintain electrical neutrality, the sum of Q from the Stern and diffuse layers represents the total charge density on the mineral grain (Leroy et al. 2008). Details on the how Q relates to the sodium sorption can be found in the Appendix B of Niu, Revil, and Saidian 2016.

Only Q was altered between trials G1-A ($Q = 3 \times 10^{-4}$ C/m^2) and G1-B ($Q = 8 \times 10^{-4}$ C/m^2). Increasing Q resulted in higher values for both σ'_{eff} and σ''_{eff}, but a greater impact is seen to σ''_{eff} (Figure 16). As expected, a higher Q represents more charge buildup and led to a more significant polarization effect. Similar results can be seen when comparing trials G6-B ($Q = 3 \times 10^{-4}$ C/m^2) and G6-C ($Q = 6 \times 10^{-4}$ C/m^2) (Figure 13). The values chosen for Q in these trials were within acceptable range for calcite, and it should be noted that Q values for clay and quartz are much higher than calcite (Niu, Revil, and Saidian 2016). Therefore, it is

possible that samples G1 and G6 contained slightly more clay content than assumed, as simulation trials performed using higher Q values (G1-B, G6-B) resulted in a better match to laboratory measurements. Our numerical simulations indicated that an increase in Q, albeit small, can have a large impact on polarization behavior and predicted σ''_{eff} values.

CONCLUSION

Our study showed how bulk electrical conductivity simulations based on digital rock imaging techniques and pore-scale complex conductivity modeling compared to laboratory measurements on carbonate reservoir rocks. For nearly all simulation trials, numerical σ'_{eff} values were below laboratory measurements, while numerical σ''_{eff} values were a closer match. The mudstone showed the most disagreement in both σ'_{eff} and σ''_{eff}, while the skeletal grainstone, with the highest degree of connectivity, showed the best match to laboratory σ'_{eff}. At least one trial from all grainstone samples generated a numerical σ''_{eff} within laboratory range. It should be noted that modern electrochemical pore-scale models assume spherical grains or pores, which might not be suitable for forward modeling on more complex, three-dimensional structures. In addition, there could be other polarization effects, e.g., membrane polarization, contributing to laboratory measurements that were not accounted for in this study. Nonetheless, some of the σ'_{eff} and σ''_{eff} values calculated in our study were a good match to laboratory results, and our input parameters were realistic. From our simulations, we learned that 1) the imaging and digital segmentation technique is important to consider, as it remains a challenge to capture interconnected microporosity due to the limits in micro-CT scanning resolutions and to build a digital microstructure that is representative of the real rock volume; 2) fundamental rock characteristics

21

such as carbonate petrology, porosity, and most importantly connectivity play a large role in the complex conductivity predictions; and 3) despite their heterogeneity, complex conductivity predictions through numerical simulations are feasible using previously established pore-scale electrical polarization models on digitally reconstructed carbonate rocks. Our results led us to a better understanding of the link between pore-scale geometrical properties and the complex conductivity response of carbonate rocks. The combined use of image-based simulation methods and laboratory MICP, SIP, and NMR inversion can help devise a more holistic approach to rock characterization (Oyewole, Saneifar, and Heidari 2016, Knackstedt et al. 2009, Bultreys, Van Hoorebeke, and Cnudde 2015, Zahid et al. 2017). This approach is more comprehensive and is especially useful in understanding more complex rocks such as carbonates. Ultimately, this can lead to improved petrophysical characterization of carbonate rocks for any reservoir or aquifer characterization project.

REFERENCES

Al-Kharusi, A. S., and M. J. Blunt. 2008, Multiphase flow predictions from carbonate pore space images using extracted network models. Water Resources Research, **44**, no. 6. doi: 10.1029/2006WR005695.

Andrä, H., N. Combaret, J. Dvorkin, E. Glatt, J. Han, M. Kabel, Y. Keehm, F. Krzikalla, M. Lee, C. Madonna, M. Marsh, T. Mukerji, E. H. Saenger, R. Sain, N. Saxena, S. Ricker, A. Wiegmann, and X. Zhan. 2013a, Digital rock physics benchmarks—Part I: Imaging and segmentation. Computers & Geosciences, **50**,25-32. doi: https://doi.org/10.1016/j.cageo.2012.09.005.

Andrä, H., N. Combaret, J. Dvorkin, E. Glatt, J. Han, M. Kabel, Y. Keehm, F. Krzikalla, M. Lee, C. Madonna, M. Marsh, T. Mukerji, E. H. Saenger, R. Sain, N. Saxena, S. Ricker, A. Wiegmann, and X. Zhan. 2013b, Digital rock physics benchmarks—part II: Computing effective properties. Computers & Geosciences, **50**,33-43. doi: https://doi.org/10.1016/j.cageo.2012.09.008.

Bazaikin, Y., B. Gurevich, S. Iglauer, T. Khachkova, D. Kolyukhin, M. Lebedev, V. Lisitsa, and G. Reshetova. 2017, Effect of CT image size and resolution on the accuracy of rock property estimates. Journal of Geophysical Research: Solid Earth, **122**, no. 5,3635-3647. doi: 10.1002/2016JB013575.

Blunt, M. J., B. Bijeljic, H. Dong, O. Gharbi, S. Iglauer, P. Mostaghimi, A. Paluszny, and C. Pentland. 2013, Pore-scale imaging and modelling. Advances in Water Resources, **51**,197-216. doi: https://doi.org/10.1016/j.advwatres.2012.03.003.

Bücker, M., and A. Hördt. 2013, Analytical modelling of membrane polarization with explicit parametrization of pore radii and the electrical double layer. Geophysical Journal International, **194**, no. 2,804-813. doi: 10.1093/gji/ggt136.

Bultreys, T., L. Van Hoorebeke, and V. Cnudde. 2015, Multi-scale, micro-computed tomography-based pore network models to simulate drainage in heterogeneous rocks. Advances in Water Resources, **78**,36-49. doi: https://doi.org/10.1016/j.advwatres.2015.02.003.

Chen, Y., and D. Or. 2006, Effects of Maxwell-Wagner polarization on soil complex dielectric permittivity under variable temperature and electrical conductivity. Water Resources Research, **42**, no. 6. doi: 10.1029/2005WR004590.

Cheng, H., and S. Torquato. 1997, Effective conductivity of periodic arrays of spheres with interfacial resistance. Proceedings of the Royal Society of London. Series A: Mathematical, Physical and Engineering Sciences, **453**, no. 1956,145.

Davis, C. A., E. Atekwana, E. Atekwana, L. D. Slater, S. Rossbach, and M. R. Mormile. 2006, Microbial growth and biofilm formation in geologic media is detected with complex conductivity measurements. Geophysical Research Letters, **33**, no. 18. doi: 10.1029/2006GL027312.

Dong, H., and M. J. Blunt. 2009, Pore-network extraction from micro-computerized-tomography images. Physical Review E, **80**, no. 3,036307. doi: 10.1103/PhysRevE.80.036307.

Duan, W., G. Zhiqian, F. Tailiang, M. Miaomiao, C. Yue, L. Yangbing, and Z. Chenjia. 2018, New Insight into the Characteristics of Tight Carbonate based on Nuclear Magnetic Resonance. Energy & Fuels, **32**, no. 3,2962-2972. doi: 10.1021/acs.energyfuels.7b03460.

Florsch, N., A. Revil, and C. Camerlynck. 2014, Inversion of generalized relaxation time distributions with optimized damping parameter. Journal of Applied Geophysics, **109**,119-132. doi: https://doi.org/10.1016/j.jappgeo.2014.07.013.

Garboczi, E. J. 1998, Finite Element and Finite Difference Programs for Computing the Linear Electric and Elastic Properties of Digital Images of Random Materials.

Johnson, D. L., J. Koplik, and L. M. Schwartz. 1986, New Pore-Size Parameter Characterizing Transport in Porous Media. Physical Review Letters, **57**, no. 20,2564-2567. doi: 10.1103/PhysRevLett.57.2564.

Karimpouli, S., and P. Tahmasebi. 2016, Conditional reconstruction: An alternative strategy in digital rock physics. GEOPHYSICS, **81**, no. 4,D465-D477. doi: 10.1190/geo2015-0260.1.

Keehm, Y., and T. Mukerji. 2004, Permeability and relative permeability from digital rocks: Issues on grid resolution and representative elementary volume, SEG Technical Program Expanded Abstracts 2004: Society of Exploration Geophysicists. 1654-1657.

Kelly, S., H. El-Sobky, C. Torres-Verdín, and M. T. Balhoff. 2016, Assessing the utility of FIB-SEM images for shale digital rock physics. Advances in Water Resources, **95**,302-316. doi: https://doi.org/10.1016/j.advwatres.2015.06.010.

Kemna, A., A. Binley, G. Cassiani, E. Niederleithinger, A. Revil, L. Slater, K. H. Williams, A. F. Orozco, F. H. Haegel, and A. Hoerdt. 2012, An overview of the spectral induced polarization method for near-surface applications. Near Surface Geophysics, **10**, no. 6,453-468. doi: 10.3997/1873-0604.2012027.

Knackstedt, M., S. Latham, M. Madadi, A. Sheppard, T. Varslot, and C. Arns. 2009, Digital rock physics: 3D imaging of core material and correlations to acoustic and flow properties. The Leading Edge, **28**, no. 1,28-33. doi: 10.1190/1.3064143.

Leroy, P., A. Revil, A. Kemna, P. Cosenza, and A. Ghorbani. 2008, Complex conductivity of water-saturated packs of glass beads. Journal of Colloid and Interface Science, **321**, no. 1,103-117. doi: https://doi.org/10.1016/j.jcis.2007.12.031.

Lin, Q., Y. Al-Khulaifi, M. J. Blunt, and B. Bijeljic. 2016, Quantification of sub-resolution porosity in carbonate rocks by applying high-salinity contrast brine using X-ray microtomography differential imaging. Advances in Water Resources, **96**,306-322. doi: https://doi.org/10.1016/j.advwatres.2016.08.002.

Lindquist, W. B., A. Venkatarangan, J. Dunsmuir, and T.-f. Wong. 2000, Pore and throat size distributions measured from synchrotron X-ray tomographic images of Fontainebleau

sandstones. Journal of Geophysical Research: Solid Earth, **105**, no. B9,21509-21527. doi: 10.1029/2000JB900208.

Mahabadi, N., S. Dai, Y. Seol, T. Sup Yun, and J. Jang. 2016, The water retention curve and relative permeability for gas production from hydrate-bearing sediments: pore-network model simulation. Geochemistry, Geophysics, Geosystems, **17**, no. 8,3099-3110. doi: 10.1002/2016GC006372.

Marshall, D., and T. Madden. 1959, Induced polarization, a study of its causes. GEOPHYSICS, **24**, no. 4,790-816. doi: 10.1190/1.1438659.

Mendelson, K. S. 1975, A theorem on the effective conductivity of a two-dimensional heterogeneous medium. Journal of Applied Physics, **46**, no. 11,4740-4741. doi: 10.1063/1.321549.

Niu, Q., M. Prasad, A. Revil, and M. Saidian. 2016, Textural control on the quadrature conductivity of porous media. GEOPHYSICS, **81**, no. 5,E297-E309. doi: 10.1190/geo2015-0715.1.

Niu, Q., and A. Revil. 2015, Connecting complex conductivity spectra to mercury porosimetry of sedimentary rocks. GEOPHYSICS, **81**, no. 1,E17-E32. doi: 10.1190/geo2015-0072.1.

Niu, Q., A. Revil, and M. Saidian. 2016, Salinity dependence of the complex surface conductivity of the Portland sandstone. GEOPHYSICS, **81**, no. 2,D125-D140. doi: 10.1190/geo2015-0426.1.

Niu, Q., and C. Zhang. 2017, Pore-scale modelling of complex conductivity of saturated granular materials. Near Surface Geophysics, **15**, no. 6,593-602. doi: 10.3997/1873-0604.2017055.

Niu, Q., and C. Zhang. 2018, Joint inversion of NMR and SIP data to estimate pore size

    distribution of geomaterials. Geophysical Journal International, **212**, no. 3,1791-1805.

    doi: 10.1093/gji/ggx501.

Oyewole, E., M. Saneifar, and Z. Heidari. 2016, Multiscale characterization of pore structure in

    carbonate formations: Application to the Scurry Area Canyon Reef Operators Committee

    Unit. Interpretation, **4**, no. 2,SF165-SF177. doi: 10.1190/INT-2015-0123.1.

Quintal, B., M. Frehner, C. Madonna, N. Tisato, M. Kuteynikova, and E. Saenger. 2011,

    Integrated numerical and laboratory rock physics applied to seismic characterization of

    reservoir rocks. The Leading Edge, **30**, no. 12,1360-1367. doi: 10.1190/1.3672480.

Revil, A. 2013, Effective conductivity and permittivity of unsaturated porous materials in the

    frequency range 1 mHz–1GHz. Water Resources Research, **49**, no. 1,306-327. doi:

    10.1029/2012WR012700.

Revil, A., N. Florsch, and C. Camerlynck. 2014, Spectral induced polarization porosimetry.

    Geophysical Journal International, **198**, no. 2,1016-1033. doi: 10.1093/gji/ggu180.

Revil, A., and P. W. J. Glover. 1997, Theory of ionic-surface electrical conduction in porous

    media. Physical Review B, **55**, no. 3,1757-1773. doi: 10.1103/PhysRevB.55.1757.

Revil, A., K. Koch, and K. Holliger. 2012, Is it the grain size or the characteristic pore size that

    controls the induced polarization relaxation time of clean sands and sandstones? : Water

    Resources Research, **48**, no. 5. doi: 10.1029/2011WR011561.

Revil, A., P. A. Pezard, and P. W. J. Glover. 1999, Streaming potential in porous media: 1.

    Theory of the zeta potential. Journal of Geophysical Research: Solid Earth, **104**, no.

    B9,20021-20031. doi: 10.1029/1999JB900089.

Saenger, E., and C. Madonna. 2011, Digital rock physics: Numerical vs. laboratory measurements, SEG Technical Program Expanded Abstracts 2011: Society of Exploration Geophysicists. 3693-3697.

Saenger, E., C. Madonna, M. Osorno, D. Uribe, and H. Steeb. 2014, Digital carbonate rock physics, SEG Technical Program Expanded Abstracts 2014: Society of Exploration Geophysicists. 2915-2919.

Sakellariou, A., T. Sawkins, T. Senden, C. Arns, A. Limaye, A. Sheppard, R. Sok, M. Knackstedt, W. Pinczewski, L. Berge, and P. ren. 2003, Micro-CT facility for imaging reservoir rocks at pore scales, SEG Technical Program Expanded Abstracts 2003: Society of Exploration Geophysicists. 1664-1667.

Schwarz, G. 1962, A theory of the low-frequency dielectric dispersion of colloidal particles in electrolyte solution. The Journal of Physical Chemistry, **66**, no. 12,2636-2642. doi: 10.1021/j100818a067.

Scott, J. B. T., and R. D. Barker. 2003, Determining pore-throat size in Permo-Triassic sandstones from low-frequency electrical spectroscopy. Geophysical Research Letters, **30**, no. 9. doi: 10.1029/2003GL016951.

Sengupta, M., M. Kittridge, and J. Blangy. 2017, Using digital rocks and simulations of pore-scale multiphysics to characterize a sandstone reservoir. Interpretation, **5**, no. 1,SB33-SB43. doi: 10.1190/INT-2016-0068.1.

Shabro, V., S. Kelly, C. Torres-Verdín, K. Sepehrnoori, and A. Revil. 2014, Pore-scale modeling of electrical resistivity and permeability in FIB-SEM images of organic mudrock. GEOPHYSICS, **79**, no. 5,D289-D299. doi: 10.1190/geo2014-0141.1.

Sogade, J., F. Scira-Scappuzzo, Y. Vichabian, W. Shi, W. Rodi, D. Lesmes, and F. Morgan. 2006, Induced-polarization detection and mapping of contaminant plumes. GEOPHYSICS, **71**, no. 3,B75-B84. doi: 10.1190/1.2196873.

Tang, D., and K. Spikes. 2017, Segmentation of shale SEM images using machine learning, SEG Technical Program Expanded Abstracts 2017: Society of Exploration Geophysicists. 3898-3902.

Vanorio, T., and G. Mavko. 2011, Laboratory measurements of the acoustic and transport properties of carbonate rocks and their link with the amount of microcrystalline matrix. GEOPHYSICS, **76**, no. 4,E105-E115. doi: 10.1190/1.3580632.

Walker, E., and P. W. J. Glover. 2018, Measurements of the Relationship Between Microstructure, pH, and the Streaming and Zeta Potentials of Sandstones. Transport in Porous Media, **121**, no. 1,183-206. doi: 10.1007/s11242-017-0954-5.

Yan, W., J. Sun, J. Zhang, N. Golsanami, and S. Hao. 2016, A novel method for estimation of remaining oil saturations in water-flooded layers. Interpretation, **5**, no. 1,SB9-SB23. doi: 10.1190/INT-2016-0074.1.

Zahid, M., D. Chunmei, A. Golab, C. Lin, X. Zhang, M. Munawar, C. Ma, X. Gee, and W. Songtaof. 2017, Pore Size Distribution and Reservoir Characterization: Evaluation for the Eocene Beach-Bar Sequence, Dongying Depression, China, International Geophysical Conference, Qingdao, China, 17-20 April 2017: Society of Exploration Geophysicists and Chinese Petroleum Society. 1213-1216.

FIGURES AND TABLES
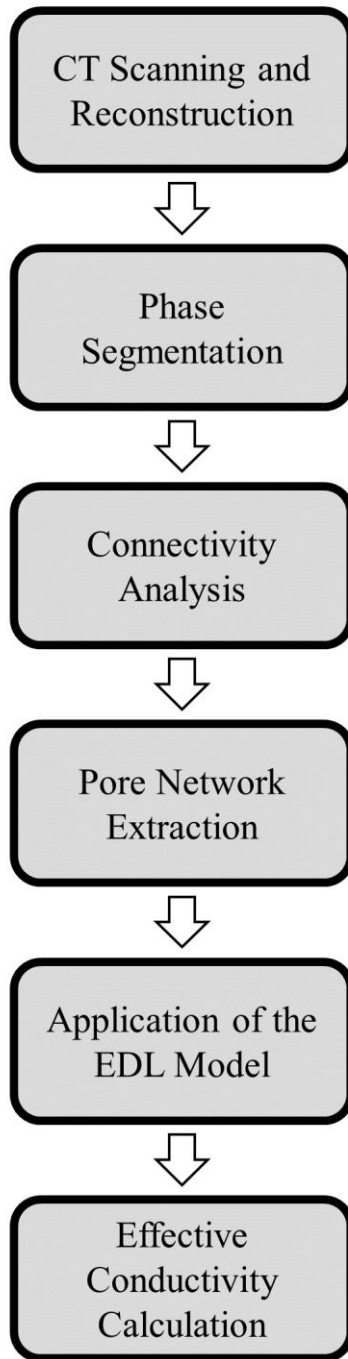
Figure 1. The workflow begins with micro-CT imaging, includes the application of our electrical

double layer and induced polarization model, and ends with the bulk conductivity calculations.

Sample	Location in Kansas	Depth (ft)	Group	Period	Lithology	Helium Porosity (%)	Permeability, k_{air} (mD)	Lens Magnification	Resolution (μm)
G1	Central	2956	Lansing-Kansas City	Upper Pennsylvanian	Grainstone	32.6	16.1	4x	4.30
G2	Central	3507	Lansing-Kansas City	Upper Pennsylvanian	Grainstone	32.2	11.9	4x	4.30
G3	Southwest	4600	Lansing-Kansas City	Upper Pennsylvanian	Grainstone	26.4	1.1	10x	1.92
G4	Central	3057	Lansing-Kansas City	Upper Pennsylvanian	Grainstone	25.6	50.4	4x	4.30
G5	Central	3099	Lansing-Kansas City	Upper Pennsylvanian	Grainstone	20.5	3.5	4x	4.30
G6	Central	3196	Lansing-Kansas City	Upper Pennsylvanian	Grainstone	14.0	19.3	4x	4.30
G7	Central	3132	Lansing-Kansas City	Upper Pennsylvanian	Grainstone	8.3	0.03	4x	4.30
G8	Central	3011	Lansing-Kansas City	Upper Pennsylvanian	Grainstone	5.7	0.01	10x	1.95
P1	South	4203	Arbuckle	Cambro-Ordovician	Packstone	7.7	27.9	10x	1.79
P2	South	4253	Arbuckle	Cambro-Ordovician	Packstone	2.8	198.9	4x	4.30
M1	South	4309	Arbuckle	Cambro-Ordovician	Mudstone	3.2	0.07	10x	1.62
M2	South	5074	Arbuckle	Cambro-Ordovician	Mudstone	11.8	5.8	4x	4.30

Table 1. Sample data and micro-CT scanning information.

Sample-Trial	Compression Criterion Number	Λ (nm)	Q (C/m^2)
M2-A	10	20	3×10^{-4}
M2-B	3	20	3×10^{-4}
G6-A	3	20	3×10^{-4}
G6-B	5	20	3×10^{-4}
G6-C	4	20	6×10^{-4}
G4-A	7	20	3×10^{-4}
G4-B	3	100	3×10^{-4}
G2-A	3	100	3×10^{-4}
G2-B	3	50	3×10^{-4}
G2-C	3	20	3×10^{-4}
G1-A	3	20	3×10^{-4}
G1-B	3	20	8×10^{-4}

Table 2. Summary of simulation trials and the input parameters chosen for each trial. These values were used in the set-up to the final effective conductivity calculation of each sample.

Figure 2. CT reconstruction of mudstone sample M2. 600 image stack with a cube edge of ~ 2.6 mm.
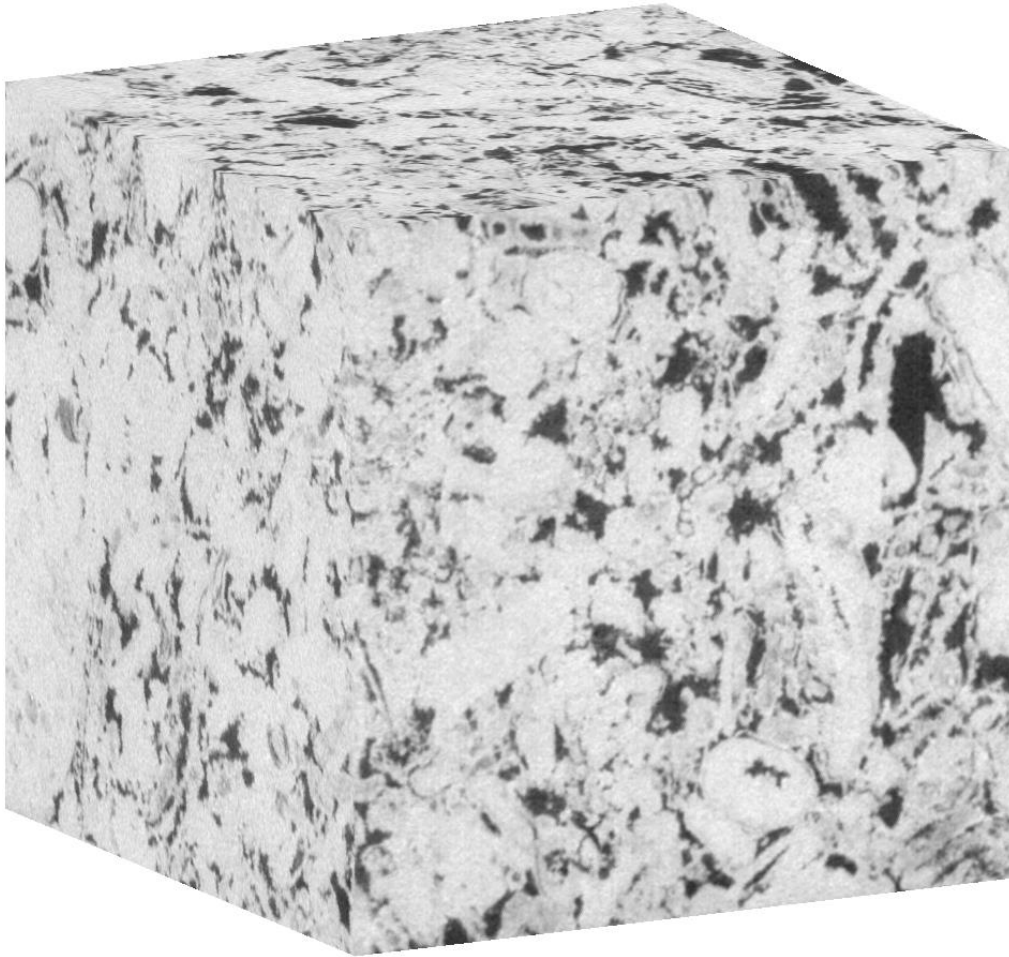
Figure 3. CT reconstruction of skeletal grainstone sample G6. 600 image stack with a cube edge of ~ 2.6 mm.
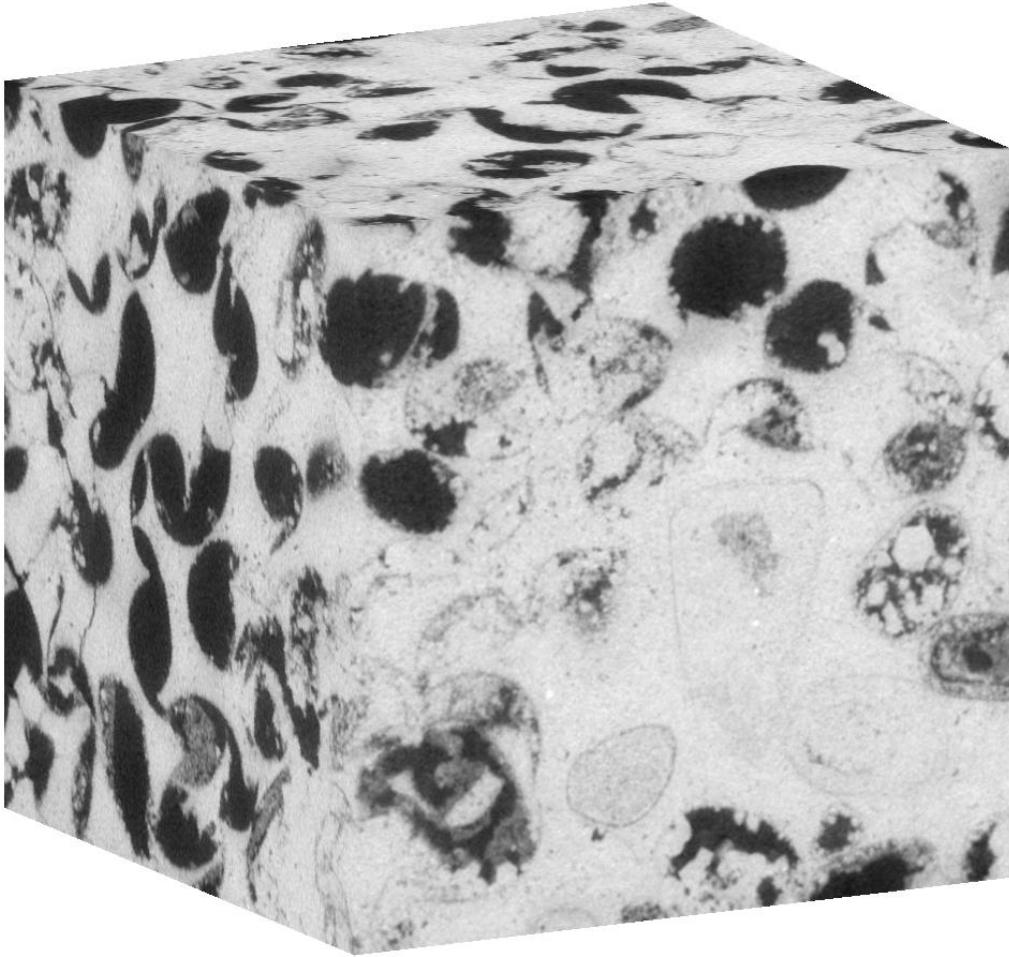
Figure 4. CT reconstruction of oomoldic grainstone sample G4. 600 image stack with a cube
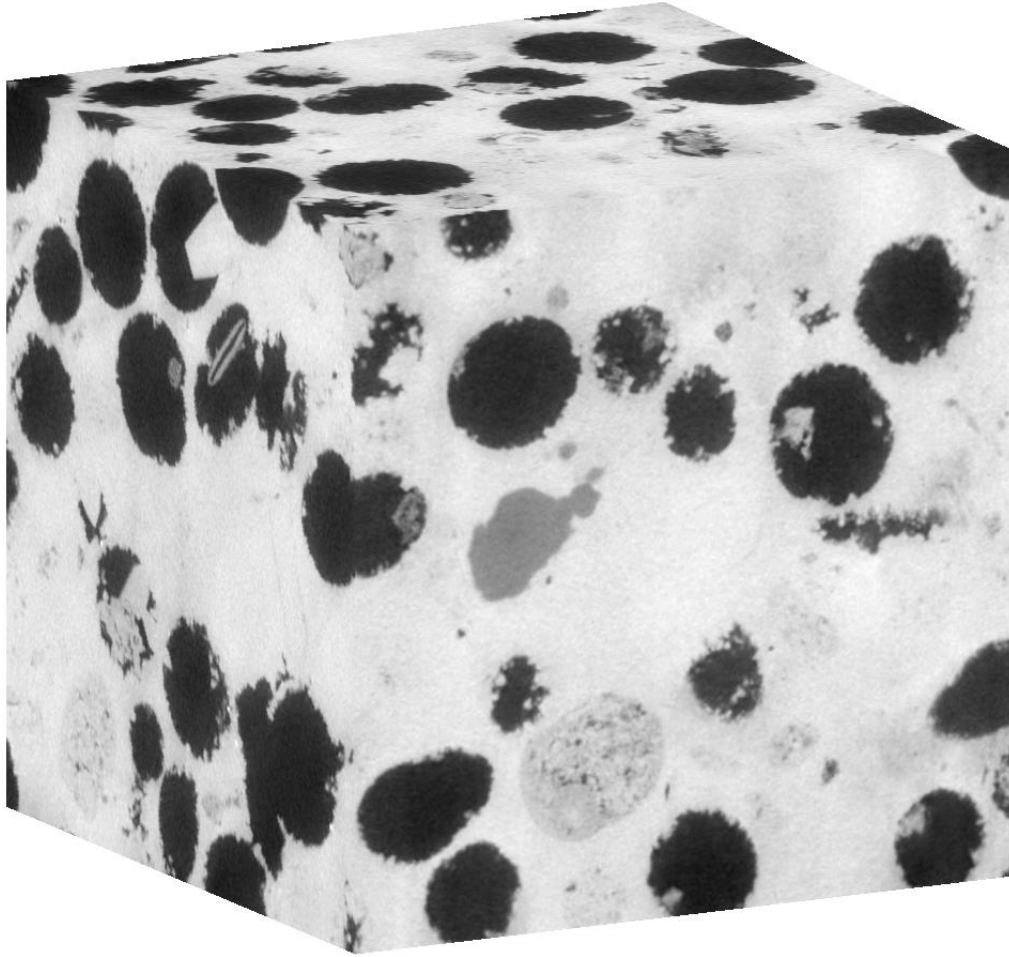
edge of ~ 2.6 mm.

Figure 5. CT reconstruction of oomoldic grainstone sample G2. 600 image stack with a cube edge of ~ 2.6 mm.

Figure 6. CT reconstruction of oomoldic grainstone sample G1. 600 image stack with a cube edge of ~ 2.6 mm.
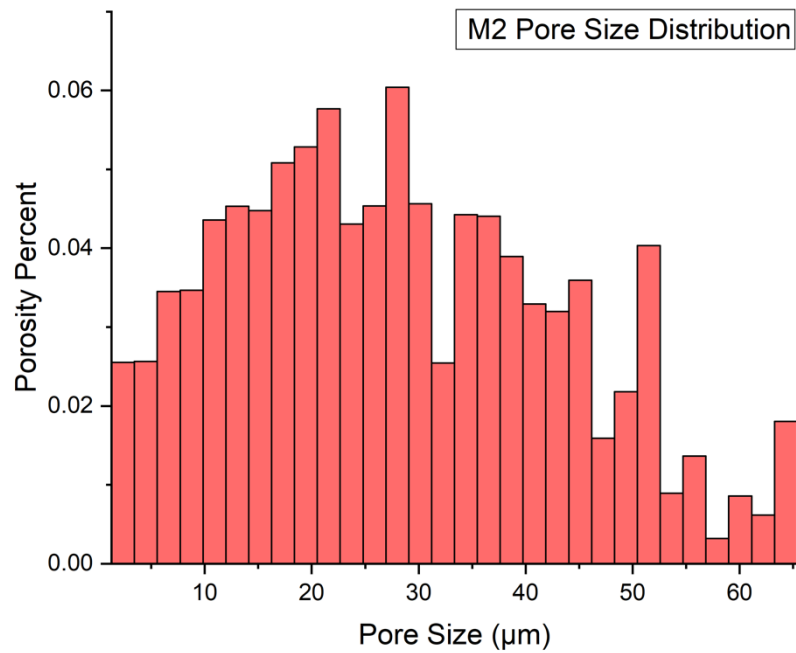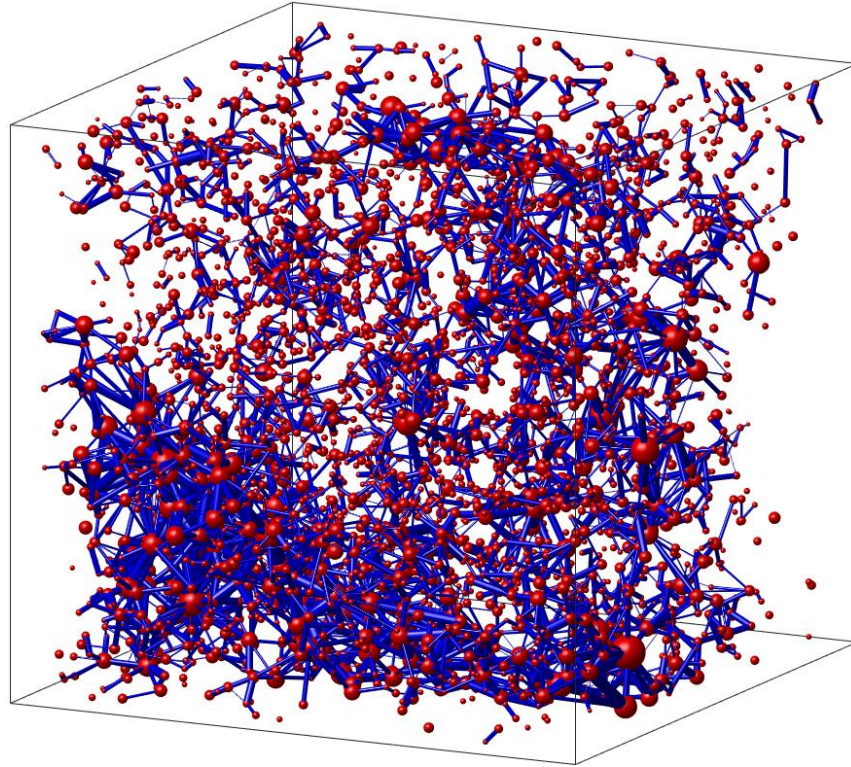
Figure 7. M2 pore network model (top) and pore size distribution (bottom). Data shown for trial M2-B with 5825 tubes and 4271 nodes.
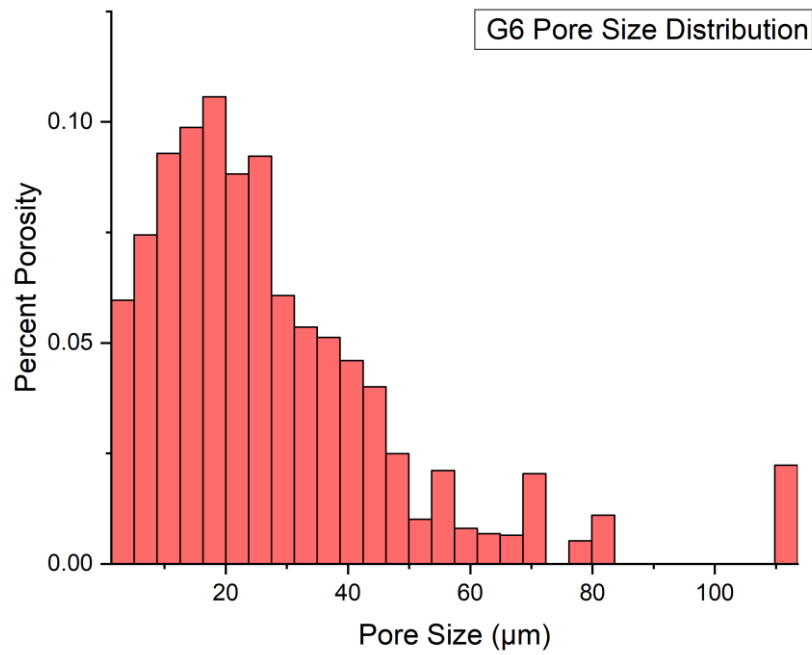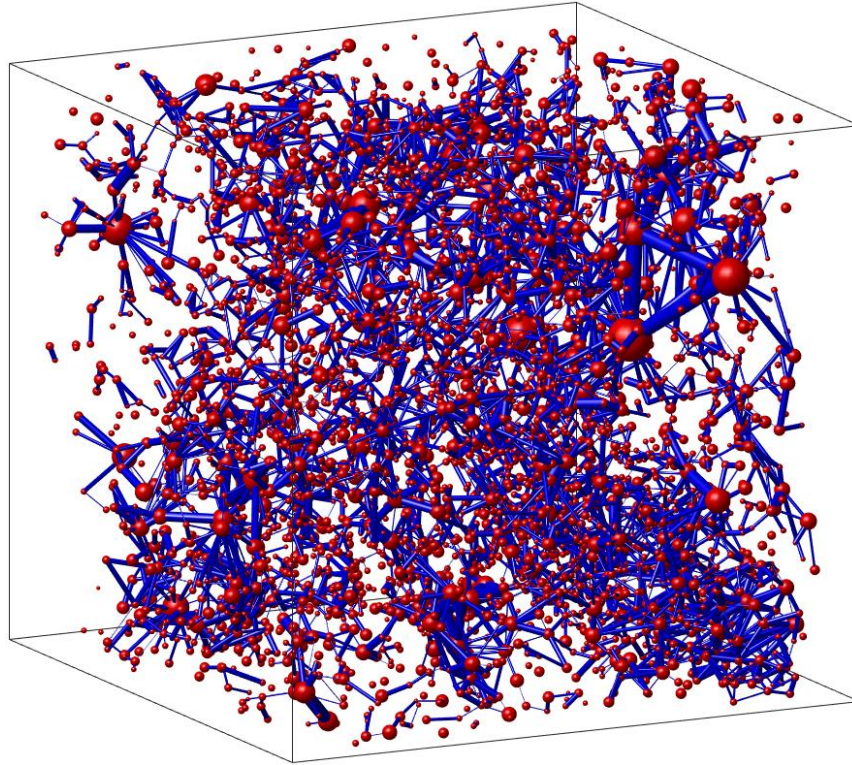
Figure 8. G6 pore network model (top) and pore size distribution (bottom). Data shown for trial

G6-A with 10265 tubes and 6052 nodes.
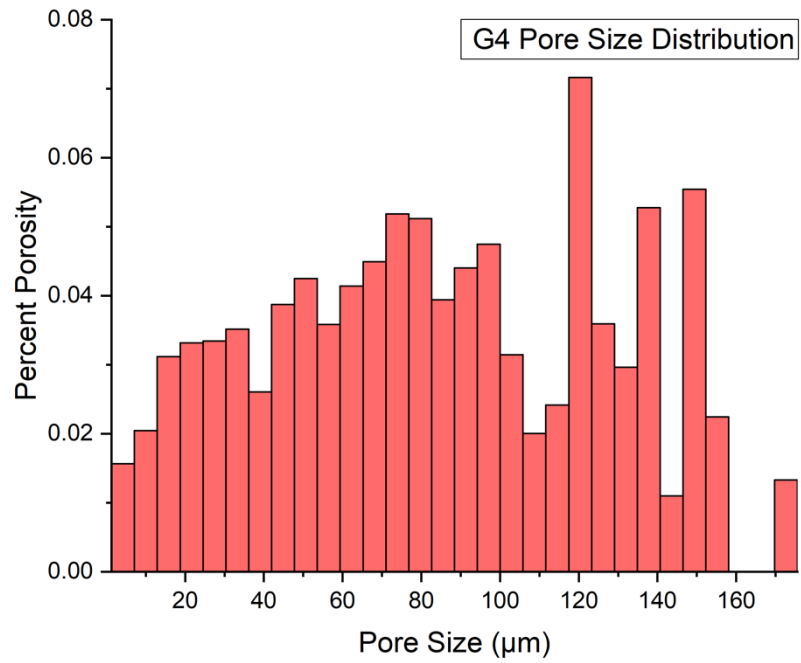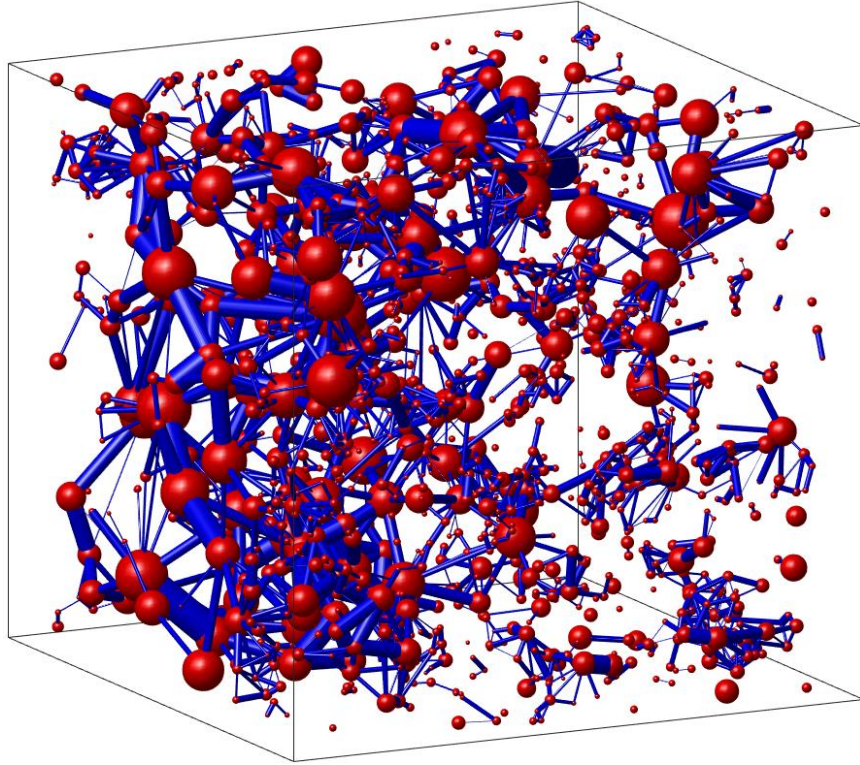
Figure 9. G4 pore network model (top) and pore size distribution (bottom). Data shown for trial
G4-A with 2242 tubes and 1364 nodes.
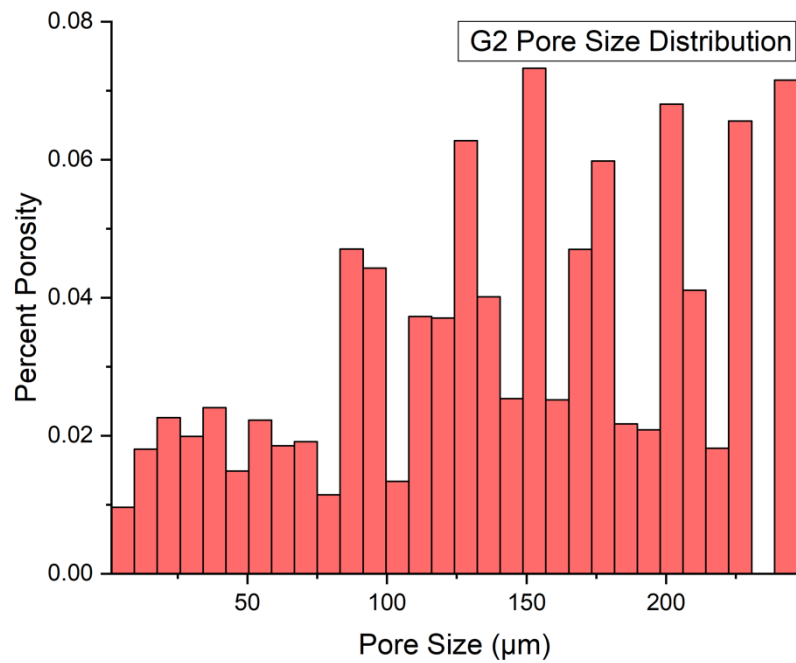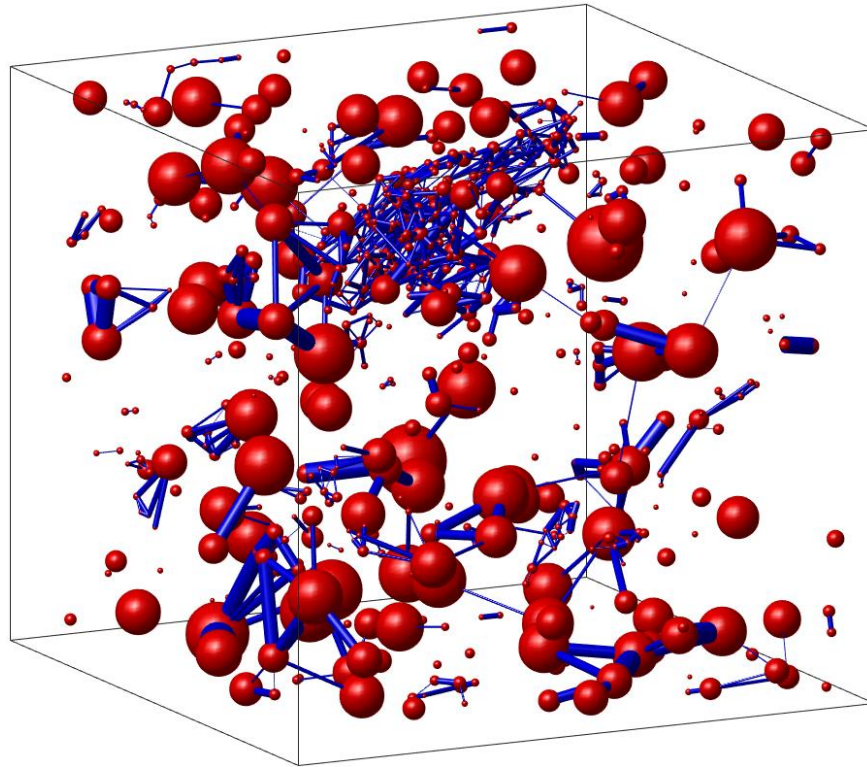
Figure 10. G2 pore network model (top) and pore size distribution (bottom). Data shown for trial

G2-A with 1176 tubes and 790 nodes.
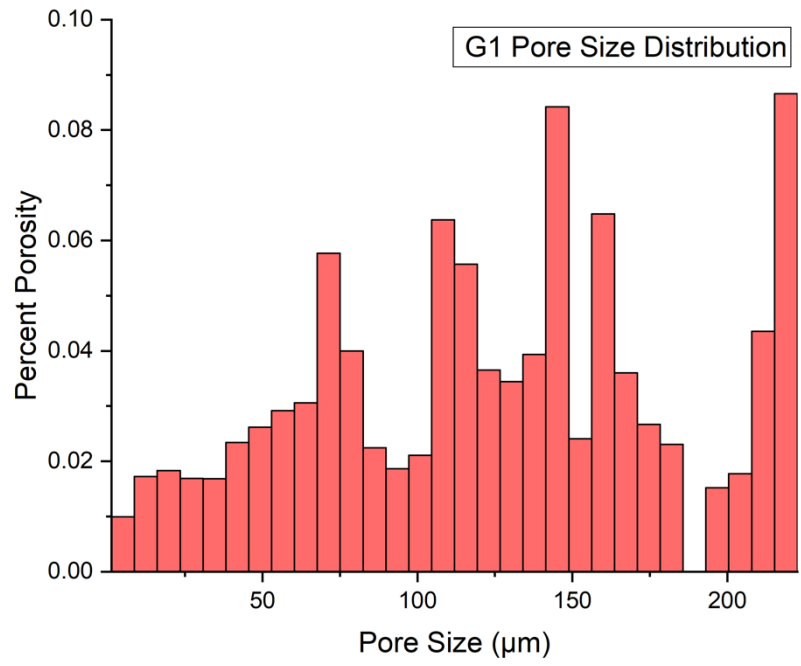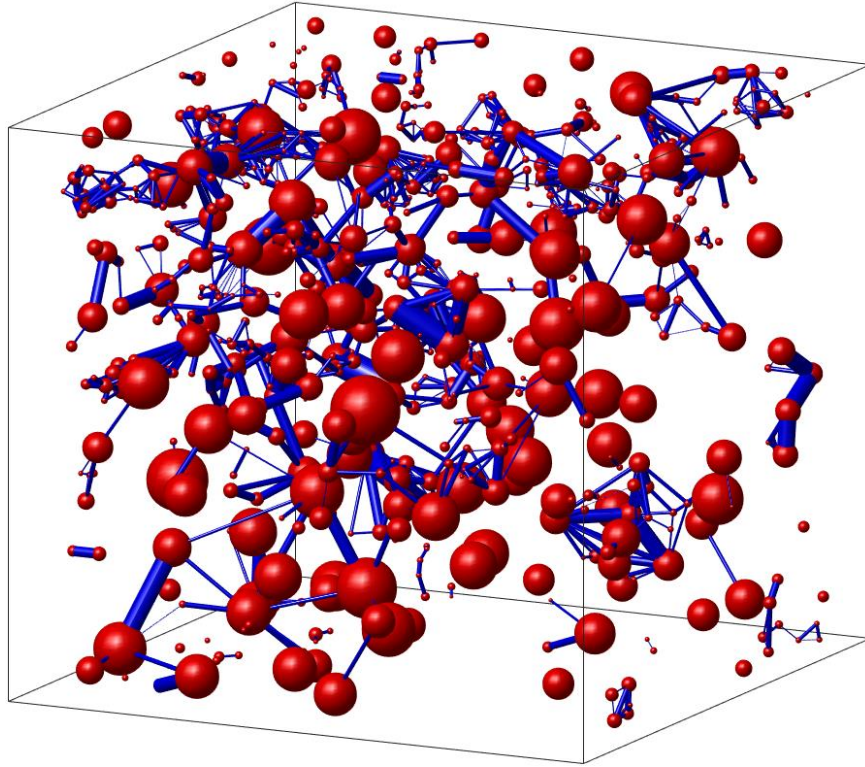
Figure 11. G1 pore network model (top) and pore size distribution (bottom). Data shown for trial
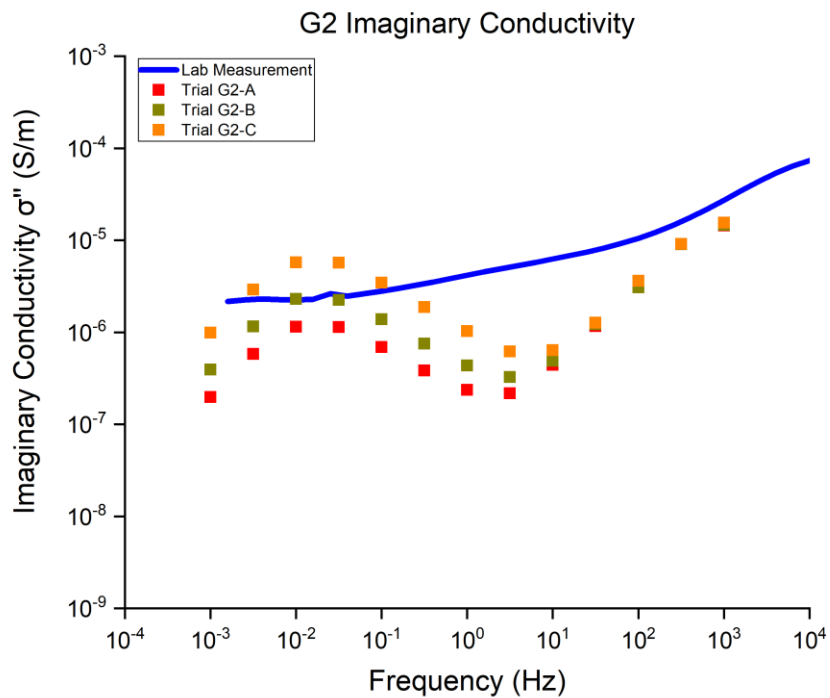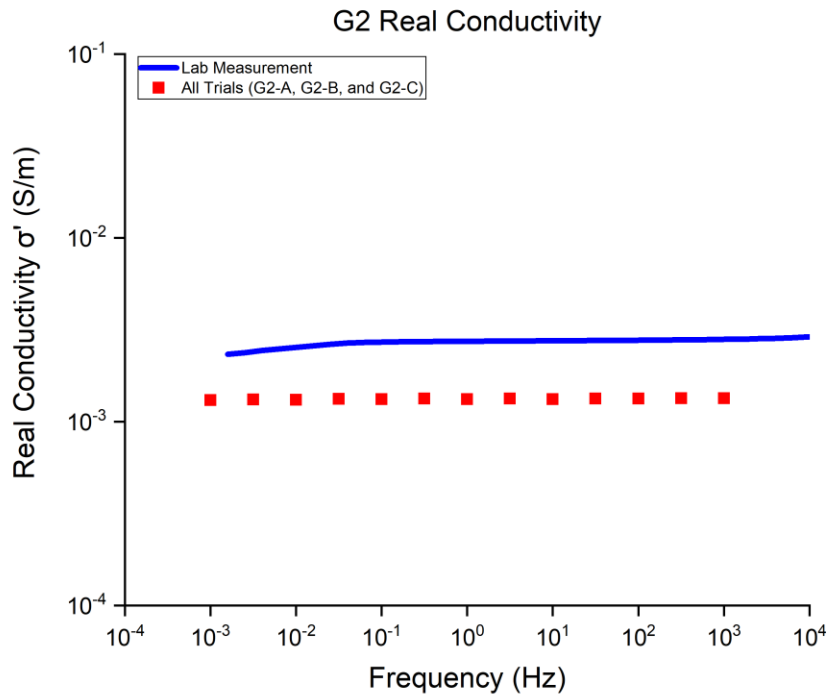
G1-A with 1363 tubes and 803 nodes.
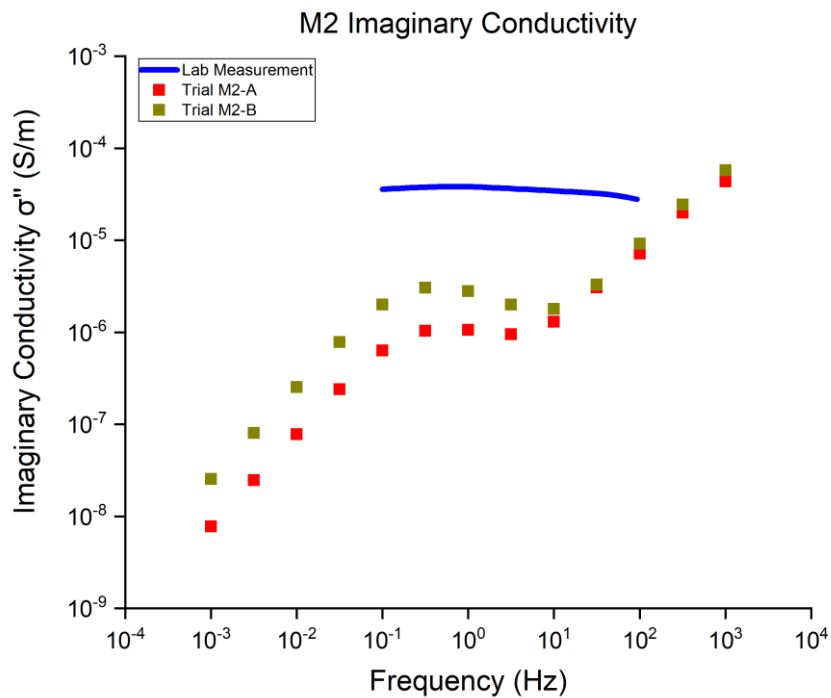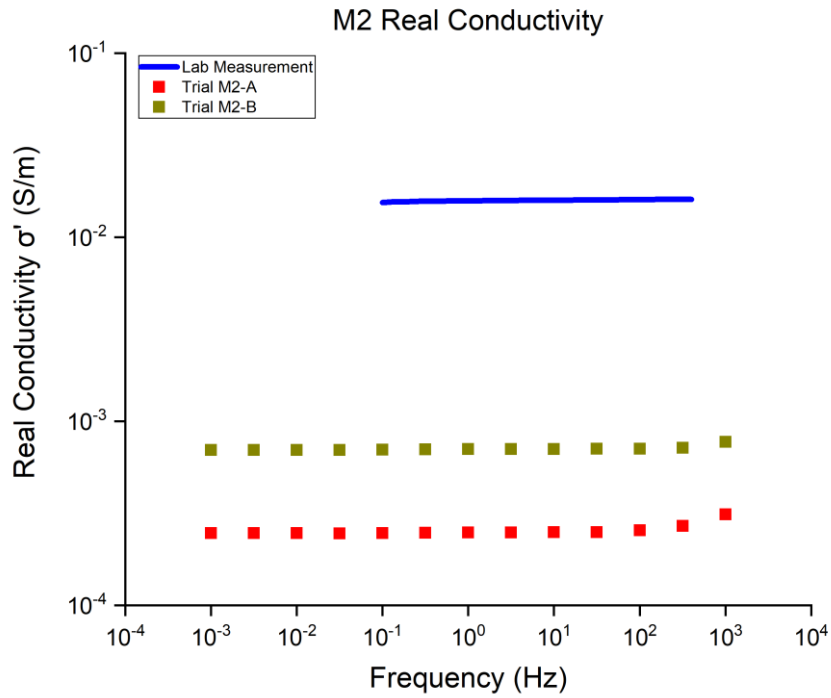
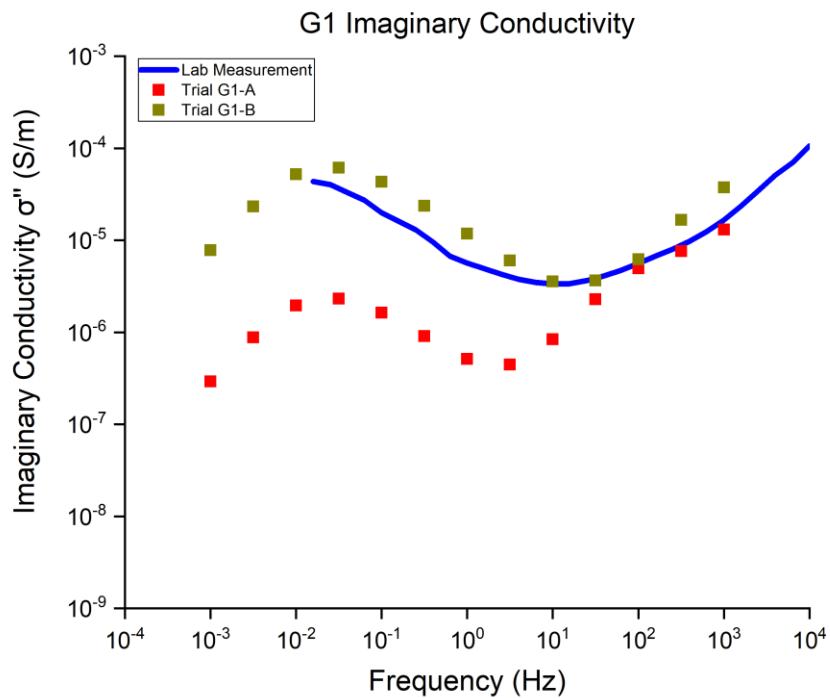Figure 12. M2 real (top) and imaginary (bottom) conductivity curves.
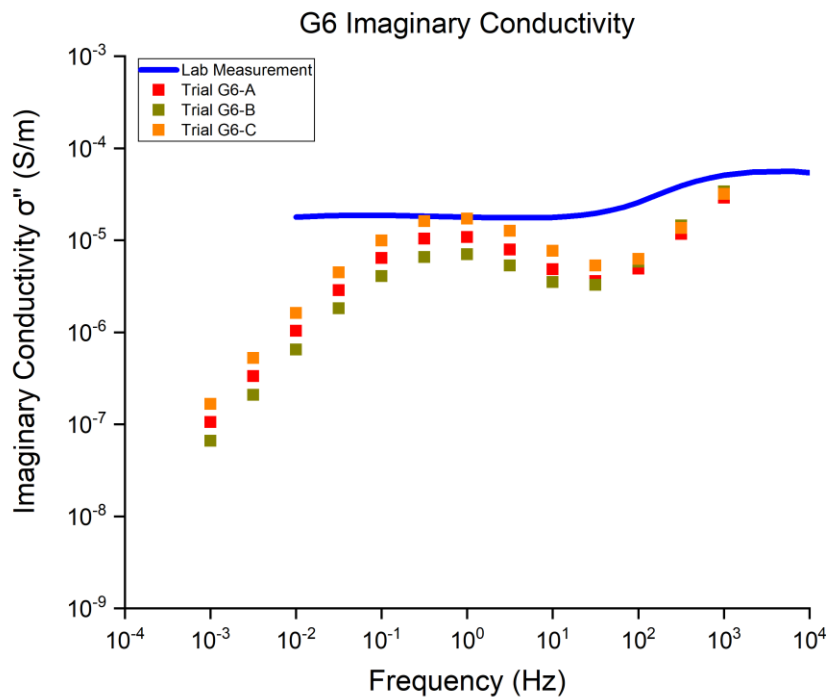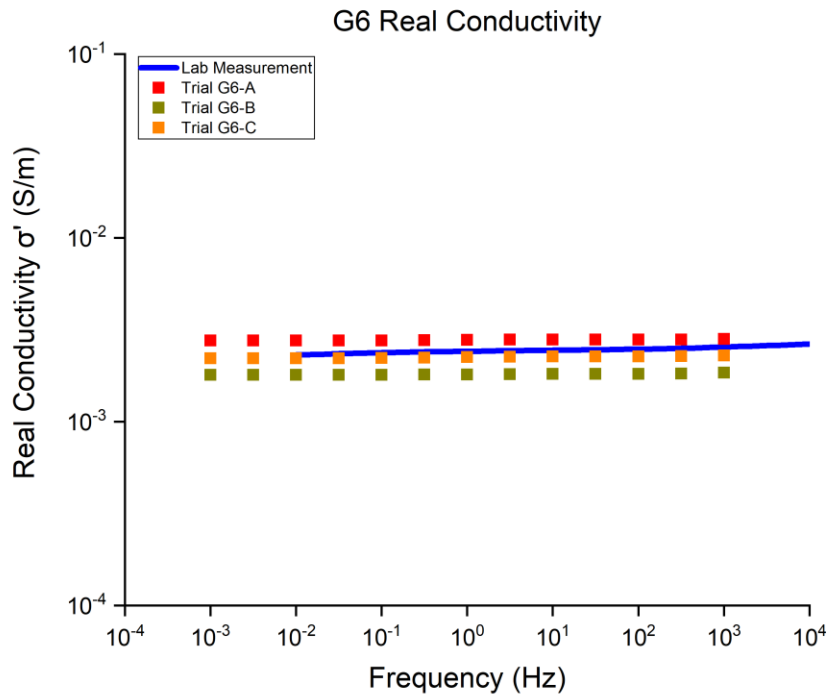
Figure 13. G6 real (top) and imaginary (bottom) conductivity curves.
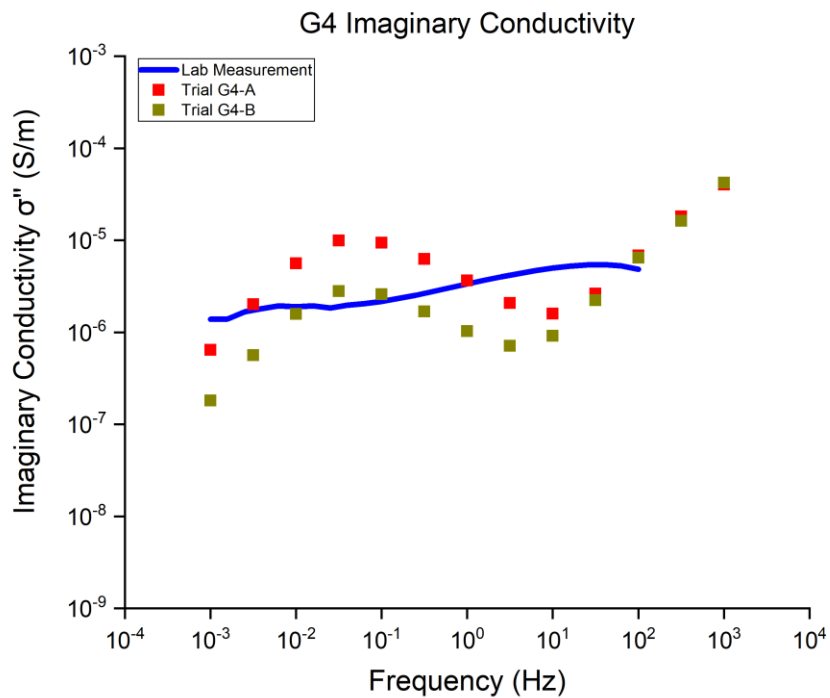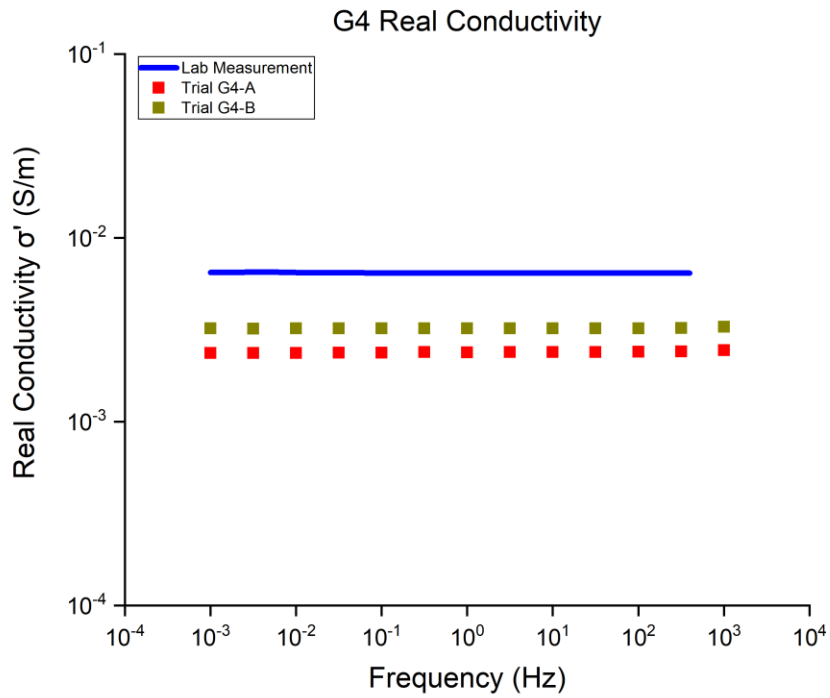
Figure 14. G4 real (top) and imaginary (bottom) conductivity curves.

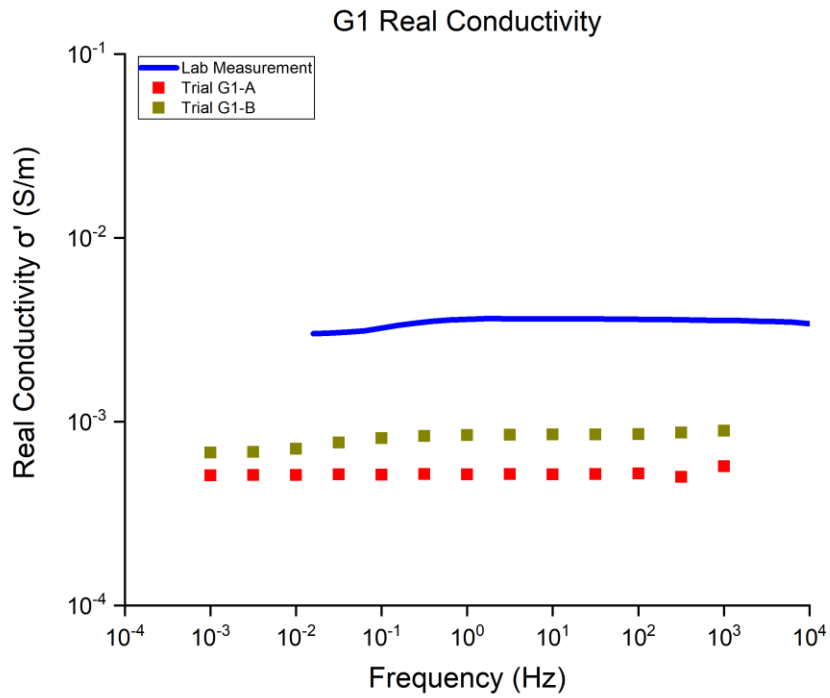Figure 15. G2 real (top) and imaginary (bottom) conductivity curves.

Figure 16. G1 real (top) and imaginary (bottom) conductivity curves.